

Visible-Light-Driven Photocatalytic Coupling of Neat Benzylamine over a Bi-Ellagate Metal–Organic Framework

Reem H. Alzard, Lamia A. Siddig, Abdalla S. Abdelhamid, and Ahmed Alzamly*

Cite This: *ACS Omega* 2022, 7, 36689–36696

Read Online

ACCESS |



Metrics & More

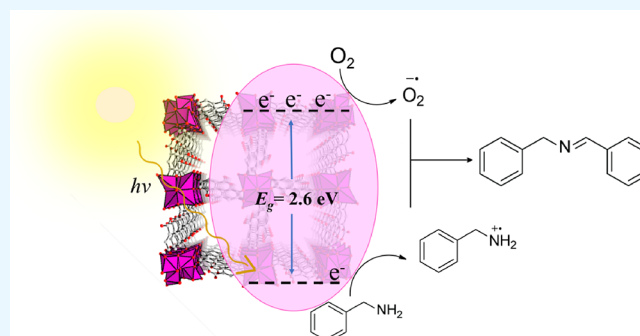


Article Recommendations



Supporting Information

ABSTRACT: Selective aerobic oxidation of benzylamine to *N,N*-benzylidenebenzylamine was achieved using a bismuth ellagate (Bi-ellagate) metal–organic framework (MOF) under simulated visible light irradiation. The bismuth ellagate photocatalyst was characterized using several spectroscopic techniques: powder X-ray diffraction (PXRD), diffuse reflectance spectroscopy (DRS), scanning electron microscopy (SEM), transmission electron microscopy (TEM), energy-dispersive X-ray spectroscopy (EDX), thermogravimetric analysis (TGA), Fourier transform infrared spectroscopy (FTIR), and nitrogen sorption measurements. Product formation was confirmed using ¹H-NMR, ¹³C-NMR, and FTIR. The photocatalytic performance of Bi-ellagate was studied for the first time, which exhibits a band gap value of 2.62 eV, endowing it with a high photocatalytic activity under visible light irradiation. The reaction product, *N,N*-benzylidenebenzylamine, was selectively obtained with a high conversion yield of ~96% under solvent-free conditions compared to other control experiments. The Bi-ellagate photocatalyst was recovered and reused four times without any significant loss in its activity, which provides an eco-friendly, low-cost, recyclable, and efficient photocatalyst for potential photocatalytic applications.



1. INTRODUCTION

The development of new routes to clean, sustainable, eco-friendly, and inexpensive energy sources is an inevitable challenge.¹ Photocatalysis is one promising technology in which new appropriate materials or systems are explored and investigated.² In this regard, solar energy is captured and used via redox reactions for practical applications such as water splitting,^{3,4} contaminant decomposition,^{5,6} CO₂ photocatalytic reduction,^{7,8} or CO₂ utilization.^{9,10} The importance of photocatalysis lies on its ability to offer green and sustainable pathways for future development,^{1,11} as well as the direct conversion of solar light without causing pollution to the environment.¹² However, some minor concerns are still associated with traditional photocatalysis as it has low efficiency,¹³ poor recyclability, a slow rate of electron transport, and limited absorption of visible light.¹⁴ For that, a wide range of attempted modification methods have been done to extend the light absorption range and reduce electron/hole recombination.^{15,16} Such methods include ion doping,^{17,18} heterojunctions,^{19,20} composite fabrication,^{21,22} and noble metal deposition.^{23,24}

Due to their chemical diversity and their robustness, inorganic semiconductors are an interesting class of photocatalysts compared to organic ones. Nonetheless, semiconductors with a distinguished photocatalytic activity may form upon electronic excitation during light-induced photocatalytic process.²⁵ Semiconductors including metals such as

bismuth,^{26,27} titanium,^{28,29} or manganese^{9,30} have been tremendously used as active photocatalysts for different applications. Among these, bismuth-based materials such as bismuth vanadate (BiVO₄),^{31,32} bismuth oxycarbonate (Bi₂O₂CO₃),³³ and bismuth oxyhalides (BiOX, X = Cl, Br, and I),^{27,34} have a superior photocatalytic activity under visible light irradiation, which is attributed to the narrow band gap energy (<3.0 eV) caused by the distributed electrons in the VB.³⁵

Another class of currently advanced materials used as photocatalysts are metal–organic frameworks (MOFs). MOFs are favored on account of their excellent structure stability, high surface area, defined diverse structure, and high tunable porosity,^{36,37} which make them potential candidates for photocatalysis.^{38–40} Particularly, bismuth-based organic frameworks (Bi-MOFs) are new attractive materials in the photocatalysis field. The combined properties of both bismuth metal and MOFs are found to highly induce photocatalytic performance.⁴¹

Received: August 3, 2022

Accepted: September 23, 2022

Published: October 4, 2022



Although there are limited publications on Bi-MOF photocatalysts, they have recently gained a lot of attention due to their diverse structure and features.⁴² As an example, bismuth-based porphyrin MOF photocatalysts exhibited 97% conversion with qualitative reaction selectivity during sulfide oxidation.⁴³ Moreover, high photodegradation activity of rhodamine B was achieved using Bi-MOFs possessing different linkers as reported by Nguyen et al.⁴⁴ Furthermore, reported Bi-MOFs constructed from 1,3,5-benzenetricarboxylic acid (H₃BTC)⁴⁵ and pyridine-2,6-dicarboxylic acid (H₂PDC)⁴⁶ linkers were used for the photodegradation of methyl orange and other organic dyes.

Considering the above, we have chosen an MOF containing bismuth and an ellagateg moiety to study its photocatalytic activity. The Bi-ellagateg MOF was chosen for its high thermal and chemical stability, which was studied over a variety of media.⁴⁷ Moreover, the light-harvesting properties of bismuth-containing compounds encourage us to investigate the photocatalytic properties of such materials.⁴⁸ Herein, we report the use of Bi-ellagateg as an active photocatalyst for the oxidative coupling of benzylamine to *N,N*-benzylidenebenzylamine under simulated visible light irradiation.

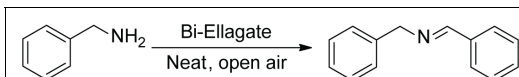
2. EXPERIMENTAL SECTION

2.1. Materials and General Procedures. Bismuth(III) acetate (C₂H₄BiO₂), ellagic acid hydrate (C₁₄H₈O₉), benzylamine (C₇H₉N), glacial acetic acid, acetonitrile (ACN), and deuterated chloroform (CDCl₃) were purchased from Sigma-Aldrich and used as received. Powder X-ray diffraction (PXRD) was recorded using a Rigaku MiniFlex benchtop X-ray diffractometer with a Cu K α radiation tube ($\lambda = 1.542 \text{ \AA}$) running at 40 kV over the range of 3–50° (2 θ) and a rate of 2 °C min⁻¹. Over the range of 4000 to 500 cm⁻¹ (512 scan average), the FTIR spectrum was obtained using ATR-IR spectroscopy (Agilent Technologies Cary 600 series FTIR spectrometer) where the background was first collected using a potassium bromide pellet and the oily product was sandwiched between two KBr disks. A Shimadzu UV-3600 spectrophotometer was used to perform UV–vis diffuse reflectance spectroscopy (DRS) of Bi-ellagateg over the range of 200 to 800 nm in which barium sulfate was first used to record the baseline. The sample surface morphology and elemental composition were analyzed using Quattro ESEM scanning electron microscopy (SEM) instrument equipped with an energy-dispersive X-ray spectroscopy (EDX) detector, which were operated at high vacuum at a 30 kV accelerating voltage. To confirm the identity of the reaction product, proton nuclear magnetic resonance (¹H-NMR) and ¹³C-NMR spectra were obtained using a Varian 400 MHz spectrometer in chloroform-d as the solvent. Finally, in an aluminum pan, the activated sample was contained, and thermogravimetric analysis (TGA) was performed on it using a Mettler Toledo TGA 2 analyzer. The surface area and porosity were examined using nitrogen sorption experiments at 77 K. The amount of gas adsorbed (cm³·g⁻¹) was shown by the N₂ adsorption–desorption isotherm as a function of relative pressure (P/P_0), where P is the N₂ equilibrium pressure and P_0 is the saturated vapor pressure at 77 K. The activated sample was first placed under vacuum for 3 h and heated at 353 K. Transmission electron microscopy (TEM) images were recorded on a high-resolution transmission electron microscope (HR-TEM) (FEI Tecnai TF-20) with a field emission gun of 200 kV.

2.2. Synthesis of Bi-Ellagateg. According to a previously reported procedure,⁴⁷ Bi-ellagateg was typically synthesized heterogeneously in a borosilicate glass beaker at room temperature. In the beaker, 0.150 g (0.495 mmol) of ellagic acid and 0.380 g of bismuth acetate (0.984 mmol) were added to a mixture of deionized water (15 mL) and 6% acetic acid (15 mL, prepared from glacial acetic acid). After adjusting the pH of the suspension solution to around 2.3, the reaction was left stirring for 48 h using PTFE stir bars. The solvent was then decanted, and the resulting solid powder was washed several times with deionized water and acetone in which it was centrifuged at 4000 rpm for 5 min after each wash. The produced Bi-ellagateg was dried and activated at 120 °C under vacuum for 6 h.

2.3. Photocatalytic Activity. The photocatalytic reaction was carried out in 25 mL round-bottom flask connected to a condenser under a normal atmosphere. An optimum of 5.0 mg (0.006 mmol) of Bi-ellagateg was added to 51 μ L (0.50 mmol) of benzylamine and stirred for 24 h while being subjected to irradiation from a 400 W halogen lamp. After the reaction was complete, the photocatalyst was washed with ACN and removed by syringe filtration. The product was purified by simple column chromatography using silica gel with ethyl acetate and hexane (1:2) to remove any possible impurities or byproducts. The solvent that contained the dissolved product was evaporated using a rotary evaporator. Finally, the isolated product (*N*-benzylidenebenzylamine) was confirmed using ¹H-NMR, ¹³C-NMR, and FTIR. All control experiments were carried out following the same procedure with required changes in some variables as outlined in Table 1.

Table 1. Photocatalytic Coupling of Benzylamine to *N*-Benzylidenebenzylamine over Bi-Ellagateg under Various Conditions^a



| Entry | Control conditions | Conversion yield (%) |
|-------|---------------------------------------|----------------------|
| I | 5 mg Bi-Ellagateg, light, no solvent | 96 |
| II | Bi-Ellagateg, with acetonitrile (ACN) | 73 |
| III | Bi-Ellagateg, no light, no heat | Nil |
| IV | Bi-Ellagateg, heat, no light | 2 |
| V | Heat, no light, no Bi-Ellagateg | Nil |
| VI | light, no Bi-Ellagateg | Nil |
| VII | 2.5 mg Bi-Ellagateg | 78 |
| VIII | 10 mg Bi-Ellagateg | 97 |

Reaction optimum conditions: 0.5 mmol (51 μ L) benzylamine, 6.4×10^{-3} mmol (5 mg) Bi-Ellagateg, open air, irradiated for 24 hours.

| entry | control conditions | conversion yield (%) |
|-------|---|----------------------|
| I | 5 mg of Bi-ellagateg, light, no solvent | 96 |
| II | Bi-ellagateg, with acetonitrile (ACN) | 73 |
| III | Bi-ellagateg, no light, no heat | nil |
| IV | Bi-ellagateg, heat, no light | 2 |
| V | heat, no light, no Bi-ellagateg | nil |
| VI | light, no Bi-ellagateg | nil |
| VII | 2.5 mg of Bi-ellagateg | 78 |
| VIII | 10 mg of Bi-ellagateg | 97 |

^aReaction optimum conditions: 0.5 mmol (51 μ L) of benzylamine, 6.4×10^{-3} mmol (5 mg) of Bi-ellagateg, open air, irradiated for 24 h.

3. RESULTS AND DISCUSSION

3.1. Characterization of Bi-Ellagate. The phase structure and purity of the activated Bi-ellagate were confirmed by comparison of the obtained PXRD diffraction pattern to the simulated one (Figure 1), which was evidence of the successful

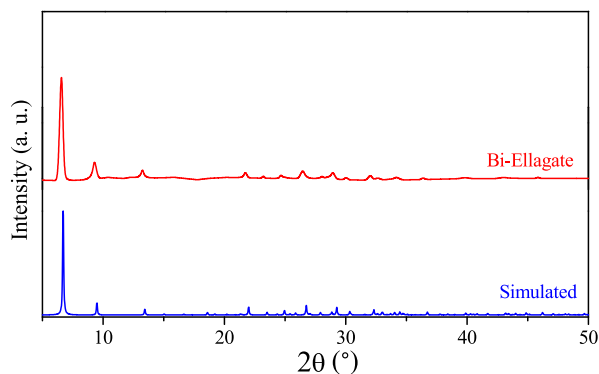


Figure 1. PXRD pattern of Bi-ellagate compared to its simulated pattern.

synthesis of Bi-ellagate. The tetragonal lattice of Bi-ellagate was identified with a $P4_2/n$ space group with cell parameters of $a = b = 18.62 \text{ \AA}$ and $c = 5.55 \text{ \AA}$.⁴⁷

The morphology of the Bi-ellagate framework was studied before and after the activation (Figure 2). The pre-activated sample had an undefined shape, which can be attributed to the presence of solvent molecules. Nonetheless, after Bi-ellagate was evacuated and activated at $120 \text{ }^\circ\text{C}$, columnar crystals were aggregated similar to the previously reported morphology (Figure 2B).⁴⁷ Furthermore, EDX analysis revealed the expected elemental composition of the sample in which bismuth, carbon, and oxygen were present as they were the only elements in the framework (Figure S1 and Table S1, Supporting Information). In agreement with the SEM images, the microscopic observations acquired by TEM (Figure 3) show elongated polydispersed crystals when the sample was dry (activated).

FTIR was used to confirm the binding mode and the coordination interaction between ellagic acid and bismuth in the solid state as shown in Figure 4. Comparing Bi-ellagate IR absorption (red spectrum) with the absorption of the linker

(blue spectrum), a clear shift in the $-\text{OH}$ band is observed from 3155 cm^{-1} (ellagic acid) to 3453 cm^{-1} (Bi-ellagate), which suggests the occurrence of a coordination interaction. Moreover, the IR band at 1517 cm^{-1} (labeled in green) in ellagic acid has disappeared in the Bi-ellagate MOF, which strongly confirms the chelation of bismuth through the hydroxyl group site of ellagic acid. The single-crystal data of Bi-ellagate reported by Grape et al. also supports this finding.⁴⁷ Other absorption bands such as the carboxylic band (1722 cm^{-1} vs 1696 cm^{-1}) was slightly affected, which further confirms the binding site at the $-\text{OH}$ group.

The thermal analysis of Bi-ellagate was conducted under a nitrogen atmosphere between room temperature and $600 \text{ }^\circ\text{C}$ (Figure S2, Supporting Information). The first drop in weight was a 12% weight loss of the material, which is attributed to water molecules from the framework pores. This was followed by the second drop, i.e., a dramatic decrease between 330 and $400 \text{ }^\circ\text{C}$ (60% weight loss), which was observed because of the decomposition of the organic linker. The decomposition of Bi-ellagate resulted with the formation of bismuth oxide (Bi_2O_3) from the remaining 40% mass. The physical change of the sample color from pale yellow to dark yellow/orange was also evidence of the MOF thermal decomposition into oxides.

From the relationship between the reflected light intensity and wavelength, the Tauc plot method¹⁹ was applied using the DRS data to calculate the band gap of Bi-ellagate (Figure 5B). The diffuse reflectance data (Figure 5A) shows a peak starting from 476.8 nm with light absorption occurring in the visible region. Estimated from a direct allowed transition, a linear fit line was extrapolated on the x axis in which the intercept was the band gap value. As shown in Figure 5B, Bi-ellagate possess a band gap of 2.6 eV ($\lambda \approx 476.8 \text{ nm}$), which makes it an active photocatalyst in the visible region.

According to Figure 6, which shows the N_2 adsorption–desorption isotherm, Bi-ellagate exhibits a type I isotherm, which is typical of a microporous material. The Brunauer–Emmett–Teller (BET) surface area was determined to be $26 \text{ m}^2 \text{ g}^{-1}$, and the Langmuir surface area was $143 \text{ m}^2 \text{ g}^{-1}$. Bi-ellagate has a pore volume of $0.08 \text{ cm}^3 \text{ g}^{-1}$ and an average pore size of 7.7 \AA .

3.2. Bi-Ellagate Photocatalytic Activity. The oxidative coupling reaction of benzylamine was selected as a model photocatalytic reaction to investigate the photocatalytic

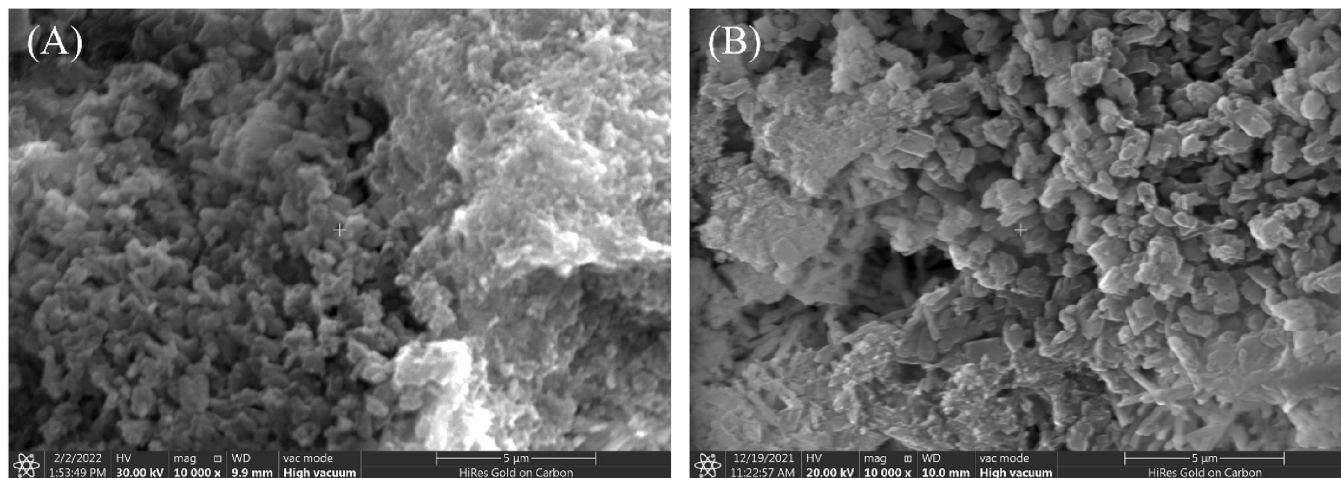


Figure 2. SEM images of the Bi-ellagate sample (A) before and (B) after activation.

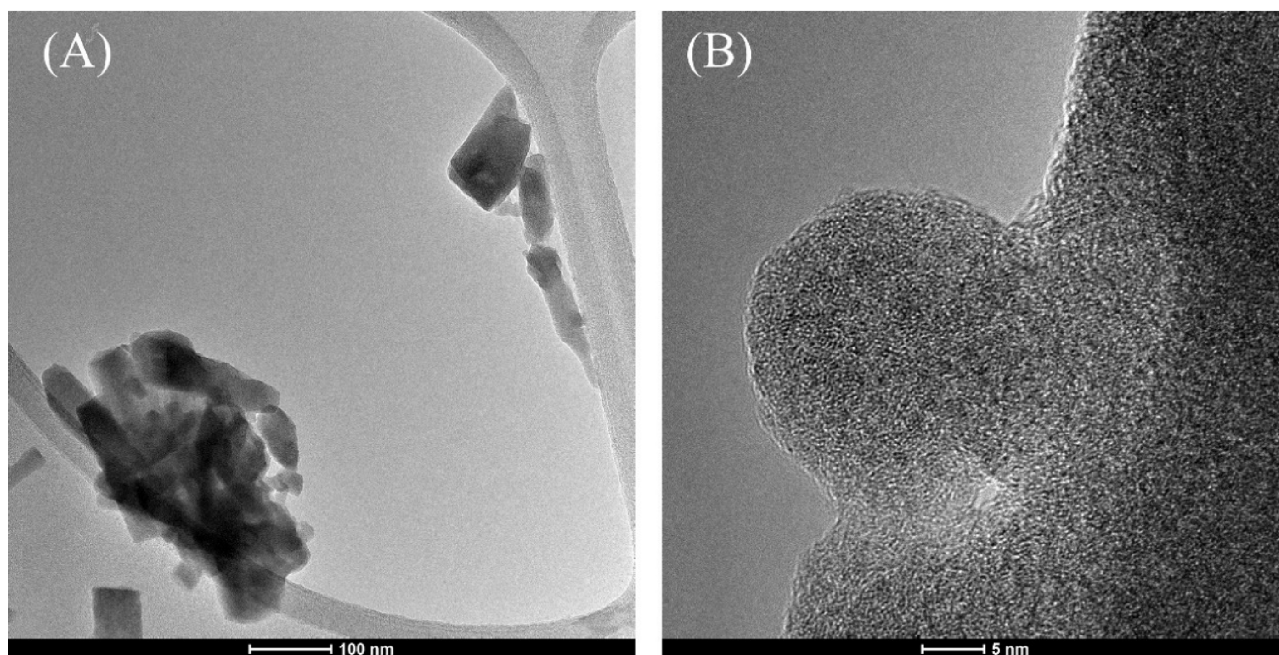


Figure 3. TEM images (scale bar = 100 nm, A) and (scale bar = 5 nm, B) of Bi-ellagate.

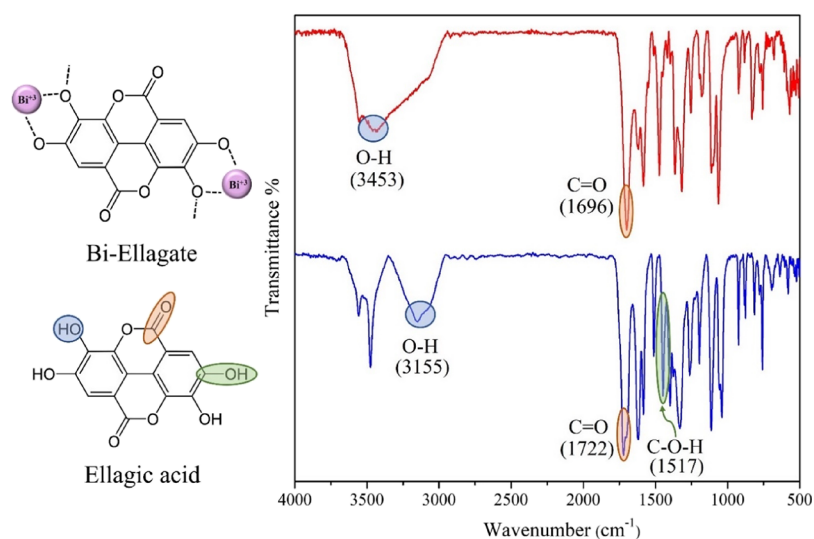


Figure 4. FTIR spectra of ellagic acid (blue) and Bi-ellagate (red) with their structures and corresponding band assignments.

performance of Bi-ellagate as it was found to have strong absorption in the visible region. *N*-Benzylidenebenzylamine was formed as a pale-yellow oily product that was first confirmed using $^1\text{H-NMR}$ and $^{13}\text{C-NMR}$ spectroscopic techniques (Figure S3, Supporting Information) where peak shifts are summarized as follows: $^1\text{H-NMR}$ (400 MHz, CDCl_3): δ 8.40 (s, 1H), 7.80–7.77 (m, 2H), 7.43–7.41 (m, 3H), 7.35–7.34 (m, 4H), 7.29–7.26 (m, 1H), 4.83 (s, 2H) and $^{13}\text{C-NMR}$ (400 MHz, CDCl_3): δ 162, 139.23, 136.09, 130.78, 128.61, 128.49, 128.27, 127.98, 126.99, 65.06. Upon the coupling of another benzylamine, the peak at 8.4 ppm is the most deshielded signal, which is also due to the generated double bond. Comparing the $^1\text{H-NMR}$ spectra of the starting material and the product, the $-\text{CH}_2$ protons of benzylamine that usually appear at 3.9 ppm are shown downfield at 4.9 ppm in *N*-benzylidenebenzylamine, indicating that it experienced a different environment, which further proves the coupling step.

In agreement with that, the $^{13}\text{C-NMR}$ data show a peak at $\delta_{\text{C}} = 65$ ppm corresponding to the environment of the two protons that are connected to $-\text{CN}$, which normally appears at a lower ppm value in benzylamine. Moreover, the carbon with the highest shift at $\delta_{\text{C}} = 162$ ppm corresponds to the product's characteristic peak of the $\text{N}=\text{C}$ bond. On the other hand, the proton signals at the aromatic region in the benzene rings of the product show a higher ppm value associated with the effect of the new environment. Having the expected shifts along with the integration of each peak, with no starting material present or byproducts, we were able to confirm a complete reaction conversion yield of 96%.

The FTIR spectrum of the product was then recorded and compared to the benzylamine spectrum from a database (NIST Standard Reference Database 35) to provide more evidence of the completion of the reaction over Bi-ellagate. The characteristic band of the $-\text{NH}$ stretch for the primary

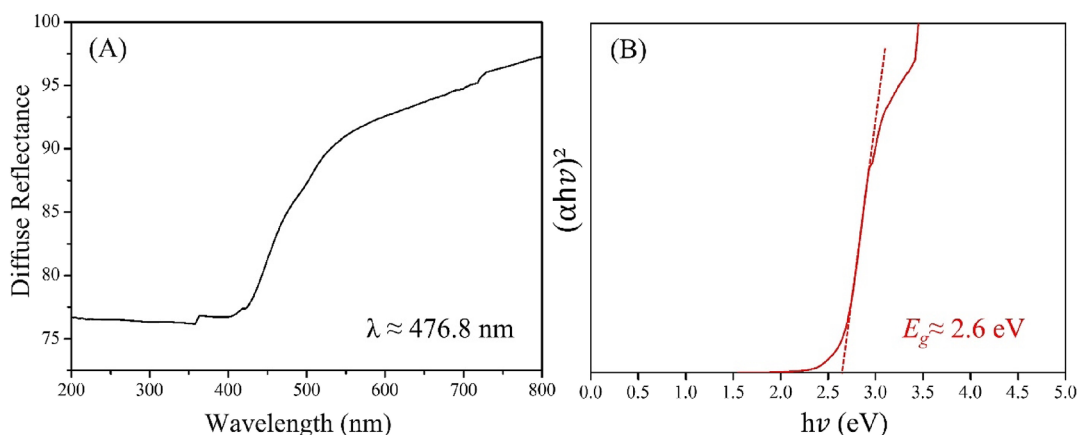


Figure 5. (A) UV–vis DRS spectra of the Bi-ellagate photocatalyst and (B) the calculated Tauc plot. The intercept at the x axis of the extended linear, red-dashed line in the graph determines the band gap value.

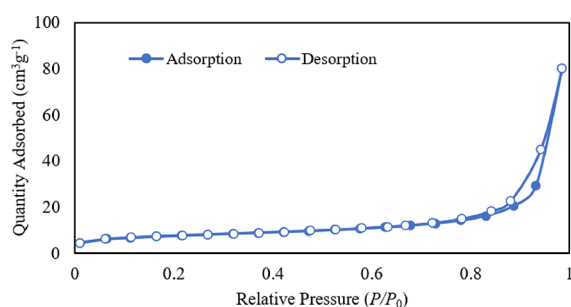


Figure 6. N_2 sorption analysis of Bi-ellagate measured at 77 K.

amine ($-NH_2$) is known to appear as a doublet between 3200 and 3500 cm^{-1} (symmetric and antisymmetric modes) in benzylamine. Upon coupling, this band has disappeared and a new band at 1643 cm^{-1} has appeared corresponding to the double bond of $C=N$ and the characteristic benzene ring bands are clearly shown between 1650 and 1800 cm^{-1} (Figure S4, Supporting Information).

To further investigate other reaction conditions, various control experiments were conducted as summarized in Table 1 and percent yields were calculated as explained in Section V in the Supporting Information. The highest yield of 96% of the *N*-benzylidenebenzylamine product was obtained in an open air and solvent-free environment, while 73% (entry II) was obtained when the reaction was completed using ACN as a solvent. This gives Bi-ellagate an additional advantage to fully proceed the reaction without the need for any solvent, as using solvents is essential for most catalysts reported for this reaction.⁴⁹ Almost all other control experiments have shown no conversion yields in the absence of either light (entries III and V) or the photocatalyst (entries V and VI), which strongly supports the high photocatalytic activity of Bi-ellagate under visible light. Studies on the photocatalyst loading effect on the conversion yield were also carried out using higher and lower photocatalyst loadings (2.5 and 10 mg) (entries VII and VIII). It was clearly apparent that the photocatalyst loading has a significant effect on the conversion yield as 78% product yield was obtained using a photocatalyst loading of 2.5 mg. However, 10 mg of the photocatalyst achieved an almost similar yield as 5 mg of the catalyst (97 and 96%, respectively), which shows that using this amount of the photocatalyst as a target is enough to enhance the photocatalytic performance of the photocatalyst.

In addition, the stability of Bi-ellagate was tested through recycling experiments under identical conditions described earlier. Before being used for the next cycle, Bi-ellagate was first separated by centrifugation, flushed with ACN, and dried in an oven at 100 °C for 2 h in which the solid Bi-ellagate was then checked and subjected to PXRD. Bi-ellagate maintained excellent photocatalytic performance with the expected product yields for four consecutive cycles (Figure S5, Supporting Information). The PXRD results (Figure 7) showed barely any difference before and after the reaction of each cycle, suggesting that Bi-ellagate is a highly stable and recyclable photocatalyst for such a reaction.

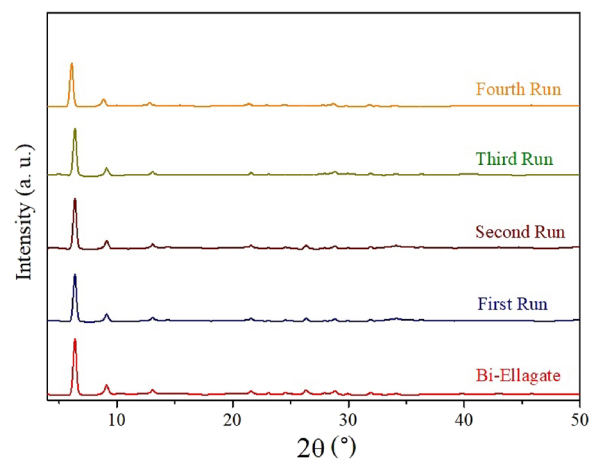
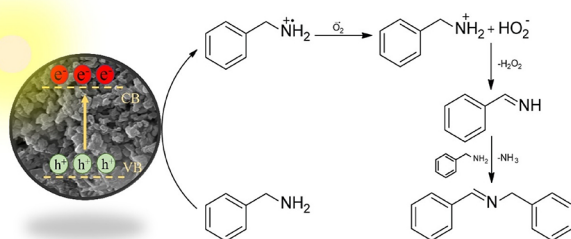


Figure 7. PXRD diffraction patterns of the recovered Bi-ellagate measured after each recycling run.

The oxidative coupling of benzylamine over Bi-ellagate is likely to proceed through an $O_2^{\bullet-}$ mediated pathway, which is proposed in Scheme 1. Upon irradiation by visible light, the photoexcited electron of the photocatalyst rises to the conduction band (CB), in which it then reacts with atmospheric molecular oxygen to produce the $O_2^{\bullet-}$ radical, which was previously confirmed using electron spin resonance (EPR) measurements.^{50–52} The adsorbed benzylamine is also oxidized by the photoinduced hole in the valence band (VB) to form an aminium radical cation intermediate. This radical cation then undergoes hydrogen-atom abstraction by the $O_2^{\bullet-}$ radical to produce phenylmethanimine ($Ph-CH_2-NH_2$),

Scheme 1. Proposed Mechanism of Benzylamine Coupling over Bi-Ellagat



therefore producing Ph-CH=NH and H₂O₂.⁵¹ The further dissociation of H₂O₂ to •OH radicals acts as supporting material for benzylamine oxidation to the produced imine, which finally reacts with another free benzylamine molecule that eventually produces the *N*-benzylidenebenzylamine product liberating ammonia.⁵⁰

The present work is the first report on the optical properties of Bi-ellagat, a photocatalyst that has been found to be active in the visible region. Thus, the photocatalytic activity of a Bi-ellagat MOF was studied for the first time since it had been first synthesized by Grape et al. Moreover, an important aspect of this coupling reaction involves using a bismuth-based MOF as a photocatalyst that can provide high conversion yields under neat conditions and using a small amount of the photocatalyst. In addition to the amine self-coupling reaction, Bi-ellagat was planned to be investigated as a photocatalyst for CO₂ cycloaddition to various epoxides in which percent activities were to be compared. Despite its robust and high stability, Bi-ellagat surprisingly failed to fulfill this role as a photocatalyst as it dissolved completely in various epoxides, resulting in a baffling pattern as revealed by PXRD. The benzylamine coupling reaction was then selected as a model reaction instead to highlight the photocatalytic potential of Bi-ellagat MOF. This present work paves the way for further investigations with different amine derivatives, which will show the catalyst's uniqueness in photocatalytic dimerization reaction.

4. CONCLUSIONS

Bi-ellagat was successfully used as a photocatalyst for the photocatalytic coupling of benzylamine to *N*-benzylidenebenzylamine. The band gap studies indicated the high potential of Bi-ellagat to work as a photocatalyst in the visible region. Rather than the traditional hydrothermal catalytic reactions that are usually done under high temperature and pressure, Bi-ellagat showed an efficient photocatalytic performance under mild reaction conditions with high photocatalytic activity and stability. The present study offers a simple, green, sustainable, and inexpensive method for utilizing solar energy for multiple applications that aim on reducing fossil fuel depletion.

■ ASSOCIATED CONTENT

Supporting Information

The Supporting Information is available free of charge at <https://pubs.acs.org/doi/10.1021/acsomega.2c04934>.

Experimental procedure, characterization data (EDX, TGA, FTIR, and recycling experiments) for Bi-ellagat and ¹H-NMR analyses of the photocatalytic reaction (PDF)

■ AUTHOR INFORMATION

Corresponding Author

Ahmed Alzamly – Department of Chemistry, UAE University, 15551 Al-Ain, UAE; orcid.org/0000-0002-7586-9785;
Email: ahmed.alzamly@uaeu.ac.ae

Authors

Reem H. Alzard – Department of Chemistry, UAE University, 15551 Al-Ain, UAE

Lamia A. Siddig – Department of Chemistry, UAE University, 15551 Al-Ain, UAE

Abdalla S. Abdelhamid – Department of Chemistry, UAE University, 15551 Al-Ain, UAE

Complete contact information is available at:

<https://pubs.acs.org/10.1021/acsomega.2c04934>

Notes

The authors declare no competing financial interest.

■ ACKNOWLEDGMENTS

This project was financially supported by the National Water and Energy Center (UAUEU, grant no. 31R238, A.A.).

■ REFERENCES

- Bhavani, P.; Hussain, M.; Park, Y.-K. Recent Advancements on the Sustainable Biochar Based Semiconducting Materials for Photocatalytic Applications: A State of the Art Review. *J. Cleaner Prod.* **2022**, *330*, 129899.
- Chen, B.; Meng, Y.; Sha, J.; Zhong, C.; Hu, W.; Zhao, N. Preparation of MoS₂/TiO₂ Based Nanocomposites for Photocatalysis and Rechargeable Batteries: Progress, Challenges, and Perspective. *Nanoscale* **2018**, *10*, 34–68.
- Luo, H.; Zeng, Z.; Zeng, G.; Zhang, C.; Xiao, R.; Huang, D.; Lai, C.; Cheng, M.; Wang, W.; Xiong, W.; Yang, Y.; Qin, L.; Zhou, C.; Wang, H.; Zhou, Y.; Tian, S. Recent Progress on Metal-Organic Frameworks Based- and Derived-Photocatalysts for Water Splitting. *Chem. Eng. J.* **2020**, *383*, 123196.
- Kranz, C.; Wächtler, M. Characterizing Photocatalysts for Water Splitting: From Atoms to Bulk and from Slow to Ultrafast Processes. *Chem. Soc. Rev.* **2021**, *50*, 1407–1437.
- Zinatloo-Ajabshir, S.; Baladi, M.; Salavati-Niasari, M. Sono-Synthesis of MnWO₄ Ceramic Nanomaterials as Highly Efficient Photocatalysts for the Decomposition of Toxic Pollutants. *Ceram. Int.* **2021**, *47*, 30178–30187.
- Mahdavi, K.; Zinatloo-Ajabshir, S.; Yousif, Q. A.; Salavati-Niasari, M. Enhanced Photocatalytic Degradation of Toxic Contaminants Using Dy₂O₃-SiO₂ Ceramic Nanostructured Materials Fabricated by a New, Simple and Rapid Sonochemical Approach. *Ultrason. Sonochem.* **2022**, *82*, 105892.
- Zhang, H.; Li, Y.; Wang, J.; Wu, N.; Sheng, H.; Chen, C.; Zhao, J. An Unprecedented Hydride Transfer Pathway for Selective Photocatalytic Reduction of CO₂ to Formic Acid on TiO₂. *Appl. Catal., B* **2021**, *284*, 119692.
- Kumar, A.; Raizada, P.; Kumar Thakur, V.; Saini, V.; Aslam Parwaz Khan, A.; Singh, N.; Singh, P. An Overview on Polymeric Carbon Nitride Assisted Photocatalytic CO₂ Reduction: Strategically Manoeuvring Solar to Fuel Conversion Efficiency. *Chem. Eng. Sci.* **2021**, *230*, 116219.
- Siddig, L. A.; Alzard, R. H.; Nguyen, H. L.; Göb, C. R.; Alnaqbi, M. A.; Alzamly, A. Hexagonal Layer Manganese Metal–Organic Framework for Photocatalytic CO₂ Cycloaddition Reaction. *ACS Omega* **2022**, *7*, 9958–9963.
- Payra, S.; Roy, S. From Trash to Treasure: Probing Cycloaddition and Photocatalytic Reduction of CO₂ over Cerium-Based Metal–Organic Frameworks. *J. Phys. Chem. C* **2021**, *125*, 8497–8507.

- (11) Davis, K. A.; Yoo, S.; Shuler, E. W.; Sherman, B. D.; Lee, S.; Leem, G. Photocatalytic Hydrogen Evolution from Biomass Conversion. *Nano Convergence* **2021**, *8*, 6.
- (12) Zhang, F.; Wang, X.; Liu, H.; Liu, C.; Wan, Y.; Long, Y.; Cai, Z. Recent Advances and Applications of Semiconductor Photocatalytic Technology. *Appl. Sci.* **2019**, *9*, 2489.
- (13) Gupta, N. M. Factors Affecting the Efficiency of a Water Splitting Photocatalyst: A Perspective. *Renewable Sustainable Energy Rev.* **2017**, *71*, 585–601.
- (14) Alismaail, S.; Ahmed, S. H.; Bakiro, M.; Alzamy, A. Photocatalytic Reduction of 4-Nitroaniline in Aqueous Solution Using BiOCl/BiOBr/RGO Ternary Heterojunction under Simulated UV-Visible Light Irradiation. *Photochem. Photobiol. Sci.* **2021**, *20*, 997–1009.
- (15) Li, Y.; Zhou, M.; Cheng, B.; Shao, Y. Recent Advances in G-C₃N₄-Based Heterojunction Photocatalysts. *J. Mater. Sci. Technol.* **2020**, *56*, 1–17.
- (16) Zhou, C.; Xia, W.; Huang, D.; Cheng, M.; Zhang, H.; Cai, T.; Xiong, W.; Yang, Y.; Song, B.; Wang, W.; Zhou, M.; Zeng, G. Strategies for Enhancing the Perylene Diimide Photocatalytic Degradation Activity: Method, Effect Factor, and Mechanism. *Environ. Sci.: Nano* **2021**, *8*, 602–618.
- (17) Ayon, S. A.; Billah, M. M.; Nishat, S. S.; Kabir, A. Enhanced Photocatalytic Activity of Ho³⁺ Doped ZnO NPs Synthesized by Modified Sol-Gel Method: An Experimental and Theoretical Investigation. *J. Alloys Compd.* **2021**, *856*, 158217.
- (18) Chakhtouna, H.; Benzeid, H.; Zari, N.; Qaiss, A. e. k.; Bouhfid, R. Recent Progress on Ag/TiO₂ Photocatalysts: Photocatalytic and Bactericidal Behaviors. *Environ. Sci. Pollut. Res.* **2021**, *28*, 44638–44666.
- (19) Hussein Ahmed, S.; Bakiro, M.; Alzamy, A. Photocatalytic Activities of FeNbO₄/NH₂-MIL-125(Ti) Composites toward the Cycloaddition of CO₂ to Propylene Oxide. *Molecules* **2021**, *26*, 1693.
- (20) Zhao, Y.; Li, L.; Zuo, Y.; He, G.; Chen, Q.; Meng, Q.; Chen, H. Reduced Graphene Oxide Supported ZnO/CdS Heterojunction Enhances Photocatalytic Removal Efficiency of Hexavalent Chromium from Aqueous Solution. *Chemosphere* **2022**, *286*, 131738.
- (21) Shi, H.; Zhao, T.; Wang, J.; Wang, Y.; Chen, Z.; Liu, B.; Ji, H.; Wang, W.; Zhang, G.; Li, Y. Fabrication of G-C₃N₄/PW₁₂/TiO₂ Composite with Significantly Enhanced Photocatalytic Performance under Visible Light. *J. Alloys Compd.* **2021**, *860*, 157924.
- (22) Zhao, C.; Wang, Z.; Li, X.; Yi, X.; Chu, H.; Chen, X.; Wang, C.-C. Facile Fabrication of BUC-21/Bi₂₄O₃₁Br₁₀ Composites for Enhanced Photocatalytic Cr(VI) Reduction under White Light. *Chem. Eng. J.* **2020**, *389*, 123431.
- (23) Hu, H.; Qian, D.; Lin, P.; Ding, Z.; Cui, C. Oxygen Vacancies Mediated In-Situ Growth of Noble-Metal (Ag, Au, Pt) Nanoparticles on 3D TiO₂ Hierarchical Spheres for Efficient Photocatalytic Hydrogen Evolution from Water Splitting. *Int. J. Hydrogen Energy* **2020**, *45*, 629–639.
- (24) Vaiano, V.; Jaramillo-Paez, C. A.; Matarangolo, M.; Navío, J. A.; del Carmen Hidalgo, M. UV and Visible-Light Driven Photocatalytic Removal of Caffeine Using ZnO Modified with Different Noble Metals (Pt, Ag and Au). *Mater. Res. Bull.* **2019**, *112*, 251–260.
- (25) Hennig, H.; Billing, R. Advantages and Disadvantages of Photocatalysis Induced by Light-Sensitive Coordination Compounds. *Coord. Chem. Rev.* **1993**, *125*, 89–100.
- (26) Chankhanittha, T.; Somaudon, V.; Watcharakitti, J.; Nanan, S. Solar Light-Driven Photocatalyst Based on Bismuth Molybdate (Bi₄MoO₉) for Detoxification of Anionic Azo Dyes in Wastewater. *J. Mater. Sci.: Mater. Electron.* **2021**, *32*, 1977–1991.
- (27) Bakiro, M.; Ahmed, S. H.; Alzamy, A. Cycloaddition of CO₂ to Propylene Oxide Using BiNbO₄/NH₂-MIL-125(Ti) Composites as Visible-Light Photocatalysts. *J. Environ. Chem. Eng.* **2020**, *8*, 104461.
- (28) Alzard, R. H.; Siddig, L. A.; Alhatti, N.; Abdallah, I.; Aljabri, L.; Alblooshi, A.; Alzamy, A. Titania Derived from NH₂-MIL-125(Ti) Metal–Organic Framework for Selective Photocatalytic Conversion of CO₂ to Propylene Carbonate. *Comments Inorg. Chem.* **2022**, *0*, 1–15.
- (29) Dharma, H. N. C.; Jaafar, J.; Widiastuti, N.; Matsuyama, H.; Rajabsadeh, S.; Othman, M. H. D.; Rahman, M. A.; Jafri, N. N. M.; Suhaimin, N. S.; Nasir, A. M.; Alias, N. H. A Review of Titanium Dioxide (TiO₂)-Based Photocatalyst for Oilfield-Produced Water Treatment. *Membranes* **2022**, *12*, 345.
- (30) Khan, I.; Sadiq, M.; Khan, I.; Saeed, K. Manganese Dioxide Nanoparticles/Activated Carbon Composite as Efficient UV and Visible-Light Photocatalyst. *Environ. Sci. Pollut. Res.* **2019**, *26*, 5140–5154.
- (31) Wang, L.; Shi, X.; Jia, Y.; Cheng, H.; Wang, L.; Wang, Q. Recent Advances in Bismuth Vanadate-Based Photocatalysts for Photoelectrochemical Water Splitting. *Chin. Chem. Lett.* **2021**, *32*, 1869–1878.
- (32) Sekar, K.; Kassam, A.; Bai, Y.; Coulson, B.; Li, W.; Douthwaite, R. E.; Sasaki, K.; Lee, A. F. Hierarchical Bismuth Vanadate/Reduced Graphene Oxide Composite Photocatalyst for Hydrogen Evolution and Bisphenol A Degradation. *Appl. Mater. Today* **2021**, *22*, 100963.
- (33) Yan, X.; Ji, Q.; Wang, C.; Xu, J.; Wang, L. In Situ Construction Bismuth Oxycarbonate/Bismuth Oxybromide Z-Scheme Heterojunction for Efficient Photocatalytic Removal of Tetracycline and Ciprofloxacin. *J. Colloid Interface Sci.* **2021**, *587*, 820–830.
- (34) Arumugam, M.; Natarajan, T. S.; Saelee, T.; Praserthdam, S.; Ashokkumar, M.; Praserthdam, P. Recent Developments on Bismuth Oxyhalides (BiOX; X = Cl, Br, I) Based Ternary Nanocomposite Photocatalysts for Environmental Applications. *Chemosphere* **2021**, *282*, 131054.
- (35) Bakiro, M.; Ahmed, S. H.; Alzamy, A. Investigation of the Band Gap Energy Shift and Photocatalytic Properties of Bi³⁺-Doped Ceria. *Inorg. Chem. Commun.* **2020**, *116*, 107906.
- (36) Yaghi, O. M.; O’Keeffe, M.; Ockwig, N. W.; Chae, H. K.; Eddaoudi, M.; Kim, J. Reticular Synthesis and the Design of New Materials. *Nature* **2003**, *423*, 705–714.
- (37) Cai, G.; Yan, P.; Zhang, L.; Zhou, H.-C.; Jiang, H.-L. Metal–Organic Framework-Based Hierarchically Porous Materials: Synthesis and Applications. *Chem. Rev.* **2021**, *121*, 12278–12326.
- (38) Wang, Q.; Gao, Q.; Al-Enizi, A. M.; Nafady, A.; Ma, S. Recent Advances in MOF-Based Photocatalysis: Environmental Remediation under Visible Light. *Inorg. Chem. Front.* **2020**, *7*, 300–339.
- (39) Dias, E. M.; Petit, C. Towards the Use of Metal–Organic Frameworks for Water Reuse: A Review of the Recent Advances in the Field of Organic Pollutants Removal and Degradation and the next Steps in the Field. *J. Mater. Chem. A* **2015**, *3*, 22484–22506.
- (40) Liu, S.; Zhang, C.; Sun, Y.; Chen, Q.; He, L.; Zhang, K.; Zhang, J.; Liu, B.; Chen, L.-F. Design of Metal–Organic Framework-Based Photocatalysts for Hydrogen Generation. *Coord. Chem. Rev.* **2020**, *413*, 213266.
- (41) Zhao, C.; Pan, X.; Wang, Z.; Wang, C.-C. 1 + 1 > 2: A Critical Review of MOF/Bismuth-Based Semiconductor Composites for Boosted Photocatalysis. *Chem. Eng. J.* **2021**, *417*, 128022.
- (42) Wang, Q.-X.; Li, G. Bi(III) MOFs: Syntheses, Structures and Applications. *Inorg. Chem. Front.* **2021**, *8*, 572–589.
- (43) Xie, D.; Wang, S.; Li, S.; Yang, W.; Feng, Y.-S. A Two-Dimensional Bi-Based Porphyrin Metal–Organic Framework Photocatalyst for White Light-Driven Selective Oxidation of Sulfides. *Catal. Sci. Technol.* **2022**, *12*, 3254–3260.
- (44) Nguyen, V. H.; Pham, A. L. H.; Nguyen, V.-H.; Lee, T.; Nguyen, T. D. Facile Synthesis of Bismuth(III) Based Metal–Organic Framework with Difference Ligands Using Microwave Irradiation Method. *Chem. Eng. Res. Des.* **2022**, *177*, 321–330.
- (45) Ye, F.; Wei, Z.-X.; Song, J.-F.; Wu, X.-H.; Yue, P. Synthesis, Characterization, and Photocatalytic Properties of Bismuth (III)-Benzene-1,3,5-Tricarboxylate. *Z. Anorg. Allg. Chem.* **2017**, *643*, 669–674.
- (46) Huang, Y.-J.; Zheng, Y.-Q.; Zhu, H.-L.; Wang, J.-J. Hydrothermal Synthesis of Bismuth(III) Coordination Polymer and Its Transformation to Nano α -Bi₂O₃ for Photocatalytic Degradation. *J. Solid State Chem.* **2016**, *239*, 274–281.
- (47) Grape, E. S.; Flores, J. G.; Hidalgo, T.; Martínez-Ahumada, E.; Gutiérrez-Alejandre, A.; Hautier, A.; Williams, D. R.; O’Keeffe, M.;

Öhrström, L.; Willhammar, T.; Horcajada, P.; Ibarra, I. A.; Inge, A. K. A Robust and Biocompatible Bismuth Ellagate MOF Synthesized Under Green Ambient Conditions. *J. Am. Chem. Soc.* **2020**, *142*, 16795–16804.

(48) Amano, F.; Nogami, K.; Tanaka, M.; Ohtani, B. Correlation between Surface Area and Photocatalytic Activity for Acetaldehyde Decomposition over Bismuth Tungstate Particles with a Hierarchical Structure. *Langmuir* **2010**, *26*, 7174–7180.

(49) Sun, D.; Ye, L.; Li, Z. Visible-Light-Assisted Aerobic Photocatalytic Oxidation of Amines to Imines over NH₂-MIL-125(Ti). *Appl. Catal., B* **2015**, *164*, 428–432.

(50) Yang, X.; Huang, T.; Gao, S.; Cao, R. Boosting Photocatalytic Oxidative Coupling of Amines by a Ru-Complex-Sensitized Metal–Organic Framework. *J. Catal.* **2019**, *378*, 248–255.

(51) Li, J.; Chang, B.; Zhao, H.; Meng, Q.; Li, M.; Han, Q. Visible-Light-Responsive Polyoxometalate-Based Metal–Organic Framework for Highly Efficient Photocatalytic Oxidative Coupling of Amines. *J. Mater. Sci.* **2021**, *56*, 6676–6688.

(52) Su, F.; Mathew, S. C.; Möhlmann, L.; Antonietti, M.; Wang, X.; Blechert, S. Aerobic Oxidative Coupling of Amines by Carbon Nitride Photocatalysis with Visible Light. *Angew. Chem., Int. Ed.* **2011**, *50*, 657–660.